Revision 1 - Word count: 7833

Jadeite and related species in shocked meteorites: Limitations on inference of shock conditions

Baziotis, Ioannis[1*], Xydous, Stamatios[1], Papoutsa, Angeliki[1], Hu, Jinping[2], Ma, Chi[2], Klemme, Stephan[3], Berndt, Jasper[3], Ferrière, Ludovic[4], Caracas, Razvan[5,6], and Asimow, Paul D.[2]

[1]Agricultural University of Athens, Natural Resources Management and agricultural engineering, Laboratory of Mineralogy and Geology, Iera Odos 75, 11855, Athens, Greece; *ibaziotis@aua.gr

[2]California Institute of Technology, Division of Geological and Planetary Sciences, Pasadena, CA 91125, USA

[3]Westfälische Wilhelms-Univ. Münster, Institut für Mineralogie, Corrensstrasse 24, 48149 Münster, Germany

[4]Natural History Museum, Burgring 7, A-1010, Vienna, Austria

[5]CNRS, Ecole Normale Supérieure de Lyon, Laboratoire de Géologie de Lyon LGLTPE UMR5276, Centre Blaise Pascal, 46 allée d'Italie Lyon 69364, France

[6]The Center for Earth Evolution and Dynamics (CEED), University of Oslo, Blindern, Oslo, Norway

ABSTRACT

Jadeite is frequently reported in shocked meteorites, displaying a variety of textures and grain sizes that suggest formation by either solid-state transformation or by crystallization from a melt. Sometimes, jadeite has been identified solely on the basis of Raman spectra. Here we argue that additional characterization is needed to confidently identify jadeite and distinguish it from related species. Based on chemical and spectral analysis of three new occurrences, complemented by first-principles calculations, we show that related pyroxenes in the chemical space $(Na)^{M2}(Al)^{M1}(Si_2)^{T}O_6 – (Ca)^{M2}(Al)^{M1}(AlSi)^{T}O_6 – (\square)^{M2}(Si)^{M1}(Si_2)^{T}O_6$ with up to 2.25 atoms Si per formula unit have spectral features similar to jadeite. However, their distinct stability fields (if any) and synthesis pathways, considered together with textural constraints, have different implications for precursor phases and estimates of impactor size, encounter velocity, and crater diameter. A reassessment of reported jadeite occurrences casts a new light on many previous conclusions about the shock histories preserved in particular meteorites.

KEYWORDS

high-pressure polymorphs; spectroscopy; planetary; pyroxenes; chondrites

INTRODUCTION

Plagioclase is common in Earth's crust and in many differentiated (e.g., shergottites and eucrites) and undifferentiated meteorites. Under the extreme temperature (*T*) and pressure (*P)* conditions that are reached during collisions on and among meteorite parent bodies, sodic plagioclase may transform into a variety of high-pressure (HP) forms, including hollandite-structured lingunite (Gillet et al. 2000; Baziotis et al. 2013; Kubo et al. 2017), amorphous maskelynite, jadeite plus a silica phase, or the recently-discovered albitic jadeite (Ma et al. 2021). In any closed-system transformation, albite that decomposes to stoichiometric jadeite must also form excess SiO_2 in the form of stishovite, coesite or an amorphous phase (James 1969; Liu 1978; Yagi et al. 1994; Kubo et al. 2010). The phase of SiO_2 that forms depends on peak pressure as well as kinetic factors (Kubo et al. 2010, 2015; Černok et al. 2017). Another transformation path, however, is from albite to albitic jadeite — a super-silicic, vacancy-rich pyroxene with excess Si occupying octahedral M1 sites (Ma et al. 2021). Tissintite, the Ca-rich analogue of albitic jadeite, forms only from more calcic plagioclase (Rucks et al. 2018); it has been found so far only in eucrites and Martian meteorites (Pang et al. 2016; Ma et al. 2015).

The presence of true stoichiometric jadeite in a given meteorite suggests that it experienced a given set of *P* and *T* conditions, especially when found in combination with a particular high-pressure silica phase, bounded by the thermodynamic equilibrium reaction albite → jadeite + SiO_2. However, it is also possible — due to kinetic reasons — to form jadeite metastably under unknown *P*-*T* conditions. In other contexts, meteoritic jadeite may occur without accompanying silica, suggesting either subsolidus recrystallization or growth from a melt. On the other hand, albitic jadeite and other minerals with related structure have similar physical properties, but

unknown and presumably different formation conditions. It is therefore critical to ensure that a meteorite contains true jadeite before using its occurrence to constrain shock conditions. It is also an important research goal to experimentally calibrate the shock conditions for the synthesis of albitic jadeite and other forms.

However, distinguishing among jadeite and its relatives is challenging. Several studies have claimed the presence of jadeite on the basis of optical petrography or Raman spectroscopy alone, without confirmation by chemical analysis or a structure-sensitive method such as electron backscatter diffraction (EBSD). One challenge is that the disorder and strain of the crystal due to substitutions and vacancies on certain cation sites can influence the stability of the crystal under irradiation by lasers, X-rays, or high-energy electron beams. Albitic jadeite, for example, is observed to be acutely sensitive to electron beams, becoming amorphous under a focused beam within a few seconds in the scanning electron microscope (SEM) (Ma et al. 2021), whereas ideal jadeite is stable and retains its structure during microanalysis with focused electron beams. A compositional analysis is clearly required to confirm the Raman identification of jadeite before the formation conditions of jadeite can be used to set a minimum pressure for a meteorite shock event. However, what are the compositional limits of the recognized jadeite-like species, and how vacancy-rich does a pyroxene have to be to qualify as albitic jadeite or tissintite? We introduce a new ternary diagram for pyroxenes in the space jadeite $[(Na)^{M2}(Al)^{M1}(Si_2)^{T}O_6]$ – kushiroite (Ca-Tschermak pyroxene) $[(Ca)^{M2}(Al)^{M1}(AlSi)^{T}O_6]$ – supersilicic pyroxene $[(\square)^{M2}(Si)^{M1}(Si_2)^{T}O_6]$ as a tool to represent the compositional ranges observed. Along with the end-members at the vertices of the ternary diagram, other notable molecules plot in this ternary space, including albite $[(Na_{0.75}\square_{0.25})^{M2}(Al_{0.75}Si_{0.25})^{M1}Si_2O_6]$,

anorthite $[(Ca_{0.75}\square_{0.25})^{M2}Al^{M1}(Al_{0.5}Si_{1.5})^{T}O_6]$, and Ca-Eskola component $[(Ca_{0.5}\square_{0.5})^{M2}AlSi_2O_6]$.

We present new combined textural, chemical, and structural data on jadeite, albitic jadeite, and related phases in shock veins from three L6 ordinary chondrites (*Ozerki*, *Chug Chug 011*, and *Chantonnay*). We then consider these observations in the context of (1) all the published references in which the presence of jadeite and its relatives were reported in chondritic meteorites and (2) new calculations of the Raman spectra of several jadeite-related high-pressure pyroxene compositions. Tissintite is only briefly considered in this work, since it has so far been observed only in achondrites (Pang et al. 2016; Ma et al. 2015). We suggest that a number of published works based on jadeite occurrences have overestimated the inferred *P-T* conditions for shocks on the L-chondrite parent body.

MATERIAL CHARACTERIZATION

Ozerki fell on 21st June 2018 in Russia and the first samples were recovered only four days after the fall. It is an L6 chondrite, moderately to strongly shocked (S4/5), without signs of weathering (W0). *Chug Chug 011* is a find, recovered in 2018 in Antofagasta, Chile; it is catalogued as L6, weakly shocked (S2; but see discussion in text), with minor signs of weathering (W1). *Chantonnay* is a historical fall (5th August 1812), classified as L6, moderately shocked (S4) and unweathered (W0) (Dodd et al. 1982b; Friedrich et al. 2004). The largest known specimen of *Chantonnay* is part of the Natural History Museum Vienna (NHMV, Austria) meteorite collection.

One polished section of *Ozerki* and of *Chug Chug 011* were investigated. Two polished thin sections of *Chantonnay* (NHMV-N9836 and NHMV-M5621) from the NHMV were analyzed. As our focus was on shock effects, we mainly studied melt

veins and melt pockets in a systematic search for shock-modified mineral grains and high-pressure polymorphs.

TEXTURE AND MINERALOGY

We used transmitted and reflected light microscopy to characterize color, texture, and likely mineralogy of phases large enough to be resolved optically. Further, we used two SEMs to characterize the texture and mineralogy of the meteorites. The Chantonnay sections were initially carbon-coated and investigated with a JEOL JSM-6610 LV instrument at the NHMV, equipped with a highly sensitive backscattered electron detector and an EDS. Analyses were conducted using 15 kV accelerating voltage and ~20 nA probe current, yielding analytical volumes with diameters less than 3 μm. Additional SEM analyses were performed at the California Institute of Technology (Caltech) GPS using a Zeiss 1550VP field-emission SEM equipped with an angle-sensitive backscattered electron detector, 80 mm^2 active area Oxford X-Max Si-drift-detector EDS, and an HKL EBSD system. SEM imaging and EDS analyses used 15 kV accelerating potential and a 120 μm field aperture in high-current mode (~4 nA probe current), yielding imaging resolution better than 2 nm and an activation volume for EDS analysis ~1–2 μm^3 on silicates. Single crystal EBSD analyses at sub-micrometer scale were performed at 20 kV and 6 nA in focused beam mode with a 70° tilted stage on uncoated specimens in "variable pressure" mode (25 Pa of N_2 gas in the chamber to reduce specimen charging). Imaging, mapping, semi-quantitative EDS analysis, and EBSD were conducted using the SmartSEM, AZtec, and Channel 5 software packages.

CHEMICAL COMPOSITION

We used two JEOL JXA-8530F Field Emission Electron Microprobes (EPMA), at the University of Muenster and at NHMV, for precise determination of the chemical

composition of the studied minerals. Both instruments are equipped with five wavelength-dispersive spectrometers (WDS) and one EDS. Mineral analyses were performed with an accelerating voltage of 15 kV. For minerals, we used a 20 nA focused beam, 20 s counting time on peak, and 10 s for each background position. For beam-sensitive minerals, we used a slightly defocused (5 μm diameter) beam, 5 nA probe current, and counting times of 10 s on-peak and 5 s on each background position. Natural mineral standards used were albite (Na, Si, Al), wollastonite (Ca), olivine (Mg), almandine (Fe), spessartine (Mn), orthoclase (K), rutile (Ti), chromite (Cr), and Ni-oxide (Ni) with ZAF matrix correction.

STRUCTURE CHARACTERIZATION

We used a FEI Nova 600 Nanolab DualBeam focused ion beam (FIB) and scanning electron microscope (SEM) for the lift-out sample preparation. The sample thinning was finalized with an 8 kV, 19 nA Ga-ion beam. The TEM analysis was performed on a FEI Tecnai TF20 with super-twin objective lens, operated at 200 kV. The EDS data were collected in TEM mode and scanning mode using a 70 μm C2 aperture and an EDAX SiLi detector. The data collection used 10 eV/channel and 51.2 μs process time, to achieve 50-500 cps signal and 20-50% deadtime. The FIB and TEM facilities are in the Kavli Nanoscience Institute at Caltech. The selected area electron diffraction (SEAD) patterns and EDS results were processed using Gatan DigitalMicrograph™ and FEI TEM Imaging and Analysis software.

RAMAN SPECTROSCOPY

A dispersive confocal Renishaw inVia Reflex Raman microscope equipped with a 514 nm Ar-ion laser at the National Hellenic Research Foundation was used with a 100× objective lens. Spectra were collected in the Stokes region for Raman shifts from 200–1600 cm^{-1}. The laser beam was spread across ~1–2 μm spots at relatively

low incident power (ca. 5 mW) to minimize sample damage. For each spot analysis, we averaged spectra over 3 consecutive 60 sec accumulation times. Gaussian-Lorentzian peak fitting was used to remove background and estimate peak center frequencies. Collected spectra were compared with published data from the RRUFF database and the Handbook of Raman Spectra. The location of each Raman spot analysis was recorded so that co-located EPMA or SEM-EDS analytical points could be collected, allowing coupled structural and compositional characterization at common spots. Raman mapping was performed on a Renishaw InVia Confocal Raman microscope at the Mineral Spectroscopy Laboratory in Caltech. The 514 nm laser was set to <2 mW power to avoid laser damage. Each spectrum in the map was collected for 5 sec with a 3000 line/mm diffraction grating, corresponding to Raman shifts of 200-1100 cm^{-1}. Color maps were produced based on the integrated area of three diagnostic peaks over a linear baseline.

RAMAN COMPUTATIONAL METHOD

We computed the theoretical Raman spectra of jadeite-related pyroxenes using density-functional perturbation theory (Gonze et al. 2005; Baroni et al. 2001; Veithen et al. 2005) as implemented in the ABINIT package (Gonze et al. 2009). The effect of the core electrons is taken into account using norm-conserving pseudopotentials (Payne et al. 1992). The electronic wavefunctions are described using planewaves, with kinetic energy cutoffs of 40 Ha (1 Ha = 27.2116 eV). The reciprocal space is sampled using a regular grid of **k** points (Monkhorst and Pack 1976). The computational methodology, including the pseudopotentials and the various parameters, was previously validated on numerous minerals and is similar to that used for the WURM project (Caracas and Bobocioiu 2011). We used a simple Gaussian

broadening to help convolve peaks and make the theoretical spectra easier to compare with the experimental ones.

RESULTS

Petrography and mineral chemistry

Ozerki. The studied thin section of *Ozerki* (see Methods section) displays two discrete areas (Fig. S1A): a light-colored chondritic lithology and a dark-colored lithology dominated by impact melt. We focused on a dense network of dark shock veins that cross-cut the light-colored lithology. The veins are variable in thickness (from 40 to 850 μm) and are locally disrupted by the presence of clasts (up to 1 mm) with angular to sub-rounded shapes. Clasts are more abundant in thicker veins and often display jigsaw-fit breccia textures. The centers of the veins contain mostly silicate clasts, whereas the margins are richer in globular metal segregations and sulfide grains. Electron probe microanalysis in *Ozerki* yields a formula for the pyroxene in the range $(Na_{0.48\text{-}0.62}Ca_{0.07\text{-}0.08}K_{0.03\text{-}0.05}Mg_{0.00\text{-}0.08}Fe_{0.00\text{-}0.02}\square_{0.25\text{-}0.40})(Al_{0.77\text{-}0.81}Si_{0.14\text{-}0.23}Fe_{0.06\text{-}0.13})Si_2O_6$, which places this pyroxene close to the albitic jadeite end-member. The Ca# [100×Ca/(Ca+Na)] ranges from 11.0 to 17.6 (Fig. S2). The albitic jadeite is found as acicular to dendritic aggregates of crystallites (up to ~4-5 μm in size) within amorphized plagioclase glass or along plagioclase-pyroxene contacts (Fig. 1). When in contact with matrix pyroxene, the crystallites display core domains with slightly higher electron backscatter brightness, grading into albitic jadeite rims with lower backscatter contrast.

Chug Chug 011. Numerous melt veins crosscut the matrix of the studied section of *Chug Chug 011* (Fig. S1B). The veins are about 100 μm wide, with central domains dominated by elongated silicate clasts oriented parallel to the margins of the veins.

215 The pyroxene is found within a zoned clast, featuring a rim of low Ca-pyroxene
216 surrounding sodic plagioclase (Fig. 2). Analysis by energy-dispersive x-ray
217 spectroscopy (EDS) yields an empirical formula $(Na_{0.49-0.64}Ca_{0.07-0.15}K_{0.03-0.05}Mg_{0.01-}$
218 $_{0.24}\square_{0.0-0.33})(Al_{0.62-0.86}Si_{0.04-0.18}Fe_{0-0.13}Mg_{0-0.21})Si_2O_6$, again close to the albitic jadeite
219 end-member. The Ca# ranges from 10 to 24. As in the *Ozerki* case, albitic jadeite
220 crystals (~1 μm long and ~200 nm wide) form a rim that completely surrounds
221 plagioclase glass (Fig. 2B).
222
223 *Chantonnay.* Three types of shock veins occur in the studied section of *Chantonnay*
224 (Fig. S1C): dark-colored clast-rich silicate veins, cross-cut by lighter-colored clast-
225 poor silicate veins, and metal-troilite veins that cross-cut both the silicate veins and
226 the wall rock (Dodd et al. 1982a). More details on the chemistry and textural
227 relationships of matrix minerals can be found in Dodd et al. (1982b). Albitic jadeite is
228 observed within a thick, dark-colored (~300 μm wide) melt vein (Figs. 2C, D). It is
229 co-located with a glassy pool and surrounded by melt vein matrix. Electron
230 microprobe analysis yields an empirical formula
231 $(Na_{0.42}Ca_{0.05}Mg_{0.11}\square_{0.42})(Al_{0.93}Si_{0.11})Si_2O_6$, with Ca# of 11, whereas EDS analyses
232 suggest a range for Ca# from 19 to 24 (Fig. S2).
233 The new compositions from all three meteorites are plotted along with
234 available data form the literature on our new ternary diagram for jadeite-related
235 pyroxenes in Fig. 3. The locations of notable molecules and end-members that plot in
236 this ternary diagram include albite $[(Na_{0.75}\square_{0.25})^{M2}(Al_{0.75}Si_{0.25})^{M1}Si_2O_6]$, anorthite
237 $[(Ca_{0.75}\square_{0.25})^{M2}Al^{M1}(Al_{0.5}Si_{1.5})^{T}O_6]$, Ca-Eskola component $[(Ca_{0.5}\square_{0.5})^{M2}AlSi_2O_6]$ and

the hypothetical molecule $\square^{M2}Si^{M1}Si_2O_6$ (described as "supersilicic pyroxene" by Smith (1984) and here called "silipyx"). On this diagram, most clinopyroxenes from the literature and from this study plot inside the Jd–Ab–Ca-Esk triangle. A few analyses plot near the Jd apex, indicating nearly pure jadeite compositions. Most reported compositions, including many assigned to jadeite on the basis of their Raman spectra, clearly display some excess Si, lying between the 2.0 and 2.25 Si atoms per formula unit (apfu) isopleths. It is possible that some of these analyses are contaminated with Si-rich matrix material due to small grain sizes or that beam-sensitive materials have lost Na, but most of the pyroxene crystals in question probably deviate significantly from the Jd–Ca-Esk join. There is no separation on this diagram among ordinary chondrite samples from different groups (LL, L, H).

The data on albitic jadeite from the current study, excluding transmission electron microscope (TEM) data from beam-sensitive material in *Chantonnay*, display consistent values of excess silica. All the *Ozerki* analyses but one have Si > 2.125 apfu, and lie close to the Si=2.25 apfu line. The *Chug Chug 011* analyses plot closer to the Si=2.125 apfu contour. Along a constant Si contour in this diagram, the fraction of vacant M2 sites increases systematically with increasing Ca content. *Ozerki* analyses have between 0.25 and 0.40 vacancies per formula unit, whereas *Chug Chug 011* analyses range between 0.09 and 0.31 vacancies. All these analyses are consistent with the definition of albitic jadeite as a solid solution with >0.10 vacancies and >2.1 Si apfu.

Raman spectroscopy

Ozerki. The Raman spectra of albitic jadeite in *Ozerki* display five distinct peaks at 376, 526, 698, 986, and 1036 cm^{-1} (Figs. 4A, 5). The predominant peak is remarkably

consistent from point to point at 698 cm^{-1}. The two peaks at higher wavenumbers related with the vibration of the $[Si_2O_6]^{4-}$ groups are visible but not as distinct or well-separated as in the ideal jadeite Raman spectrum (Figs. 4A, 5).

Chug Chug 011. We acquired numerous spectra from the area hosting albitic jadeite crystals in *Chug Chug 011*. The predominant peak is near 698 cm^{-1} but is shifted to lower wavenumbers (~693 cm^{-1}) in some spectra. Moreover, the typical jadeite peak at 1038 cm^{-1} is shifted to 1016 cm^{-1}, which may be associated either with a diopside-related structure or another HP clinopyroxene (Figs. 4A, 5). The low-wavenumber peak typically seen at 376 cm^{-1} is shifted to somewhat higher wavenumbers (~388 cm^{-1}).

Chantonnay. The Raman spectrum of albitic jadeite in *Chantonnay* displays three major peaks at 377, 699, and 1038 cm^{-1} alongside less intense peaks at 222, 254, 328, 522, and 987 cm^{-1} (Fig. 4A). The peak positions closely match the reference spectrum of jadeite (RRUFF ID_R050220) in the RRUFF database (Lafuente et al. 2015), but many of them have modestly broader line shapes. This broadening may be associated either with crystals that are small compared to the Raman spot diameter or to cation disorder in the albitic jadeite structure.

DISCUSSION

Raman spectrum of jadeite: theory and reality

The Raman spectrum of jadeite is well-characterized from high-quality terrestrial specimens and density-functional theory calculations (Prencipe 2021; Prencipe et al. 2014). It has strong characteristic A_g symmetry peaks associated with the silicate

chains at ~377, ~700, ~990, and ~1037 cm^{-1} as well as bands associated with octahedral site vibrations at ~203, 328, and 528 cm^{-1}. The experimental Raman spectrum of tissintite is quite similar, though peak shifts relative to jadeite are large enough to observe a difference with strong peaks at ~377, 693, and 997 cm^{-1}, and with less intense peaks at ~203, 415, 523, and 573 cm^{-1}. The ~1037 cm^{-1} peak is absent. These Raman features are consistent with both experimental and simulation results for a *C2/c* clinopyroxene (e.g., Prencipe et al. 2014; Yang et al. 2009; Caracas and Bobocioiu 2011). However, all the Raman bands of tissintite become progressively broader with increased substitution of (Si^{4+}+Mg^{2+}) for octahedral Al^{3+} and increased cation and vacancy disorder on the M2 site (Ma et al. 2015). In supersilicic jadeites, such as albitic jadeite, the presence of octahedral Si is associated with the observation of new Raman peaks at ~340, 596, and 1110 cm^{-1} (Yang et al. 2009).

We have computed theoretical Raman spectra for phases similar in structure to jadeite, but spanning a compositional range encompassing that observed in the three meteorites: ordered albitic jadeite $(Na_{0.75}\square_{0.25})^{M2}(Al_{0.75}Si_{0.25})^{M1}(Si_2)^{T}O_6$, jadeite$_{50}$albite$_{50}$ $(Na_{0.875}\square_{0.125})^{M2}(Al_{0.875}Si_{0.125})^{M1}(Si_2)^{T}O_6$, jadeite, $(Na)^{M2}(Al)^{M1}(Si_2)^{T}O_6$, tissintite $(Ca_{0.75}\square_{0.25})^{M2}(Al)^{M1}(Al_{1.0}Si_{1.0})^{T}O_6$, kushiroite (i.e., Ca-Tschermak pyroxene) $(Ca)^{M2}(Al)^{M1}(Al_{1.0}Si_{1.0})^{T}O_6$, and silipyx $(\square)^{M2}(Si)^{M1}(Si_2)^{T}O_6$ (Fig. 4B-G). The results of the jadeite simulation are in good agreement with the measured spectra for jadeite (RRUFF ID_R050220). Computed peaks are slightly shifted relative to measured frequencies, as is normally the case with density functional theory (DFT) calculations (Caracas and Bobocioiu 2011;

311 Gonze et al. 2005). The other spectra have similar patterns, typical of pyroxenes, and
312 the differences among them can be quite subtle.

313 The computed spectrum of pure jadeite has a set of broad peaks at low
314 frequencies, in three groups: 192, 195, and 210 cm^{-1}; 243, 273, 289, and 313 cm^{-1};
315 and the most intense peaks in this region at 353, 371, and 372 cm^{-1}, with a shoulder at
316 414 cm^{-1}. These peaks are dominated by various bending movements of tetrahedra
317 acting as rigid bodies. M2 cations like Na and Ca participate in these low-frequency
318 modes, but their presence is more significant in infrared-active modes in the same
319 frequency range. In non-centro-symmetric structures, which develop due to ordering
320 of vacancies, M2 cations contribute to the broadening of these sets of low-
321 wavenumber peaks. The spectra of all the pyroxenes computed here share these three
322 sets of peaks and their absolute and relative intensities are all similar. It is very
323 unlikely that the peaks below 450 cm^{-1}, whether computed or measured, can be used
324 to reliably distinguish the cation proportions or to quantify the number of vacancies.

325 Next, there is a broad weak peak due to the cation on the M2 site moving
326 against the sublattice of oxygen atoms, centered at 502 cm^{-1} in jadeite, at 591 cm^{-1} in
327 albitic jadeite, and at 648 cm^{-1} in silipyx. This mode occurs in other high-pressure
328 minerals with octahedral silica, like akimotoite (Imae and Ikeda 2010) and post-
329 perovskite, where it is the most intense mode (Caracas and Cohen 2006). In
330 pyroxenes, although the peak center is quite composition dependent, this mode is
331 unlikely to be clearly observed experimentally due to its low intensity and diffuse
332 peak shape.

333 The most intense Raman peak, typical of pyroxenes, is calculated at 572 cm^{-1}
334 in pure jadeite and at 638 cm^{-1} in kushiroite. The addition of vacancies on the M2 site
335 leads to a nearly linear upward shift in the frequency of this mode, to 701 cm^{-1} in

albitic jadeite and 729 cm^{-1} in silipyx. This mode is dominated by the breathing of the $(M2)O_6$ octahedra. At still higher frequencies one finds weak modes due to breathing of the SiO_4 tetrahedra; in some compositions these modes vanish almost completely (Fig. S3).

In summary, computed and observed Raman spectra show that the number of vacancies and the identity of the M1 cations influence peak positions and relative intensities. However, in practice, distinguishing between jadeite and related minerals using Raman spectra likely requires rather idealized observational conditions, with the laser focused onto a single crystal large enough to exceed the spot diameter (typically at least ~1-2 μm). In shocked meteorites, especially in those shocked heavily enough to contain significant amounts of jadeite, the rapidly grown HP polymorphs typically occur mostly as tiny crystals or as aggregates of crystallites from a few nm up to rarely more than ~2 μm in size. Furthermore, as a rule, HP phases often occur as intergrown composites of various polymorphs. As such, Raman spectra acquired from natural shock melt veins in meteorites are often of relatively poor quality, with broadened peaks, low intensities leading to missing peaks, and mixed-phase excitation. This means that the distinctive differences between true jadeite and defective pyroxenes like tissintite and albitic jadeite are challenging to observe. Indeed, there are a number of published cases where spectra with only a few (perhaps only one) of the main jadeite peaks and significant peak broadening are reported but have nevertheless been interpreted specifically as evidence of the presence of jadeite (Bazhan et al. 2017a; Feng et al. 2017).

Stability under electron beam irradiation

As seen in previous studies, many minerals, especially those that are metastable at ambient conditions, quickly become amorphous when exposed to an electron beam at the current and voltage typically used in SEM and EPMA instruments (for example, bridgmanite; Tschauner et al. 2014). Stoichiometric jadeite is not beam-sensitive; it continues to yield high-quality EBSD patterns under extended irradiation. The two recently identified high-pressure vacancy-rich pyroxenes (i.e., tissintite and albitic jadeite) respond in different ways to the electron beam. Despite having about one-quarter of the M2 sites vacant, tissintite is not beam sensitive[14]. On the other hand, albitic jadeite, which also has excess Si on the M1 site, is highly beam sensitive[4,5]. If Si on the M1 site were the sole factor governing beam stability, all the albitic jadeite reported here would presumably show similar behavior, as all three cases have ≥0.10 Si on M1 site. However, the albitic jadeite in *Ozerki* is beam-stable; we collected quality EBSD patterns from this occurrence with no special beam exposure precautions (Figs. 6A, B). In contrast, the albitic jadeite in *Chantonnay* and *Chug Chug 011* are both beam-sensitive; EBSD contrast disappeared within seconds of switching to a fixed beam spot (Figs. 6C, D). It seems, therefore, that the *Ozerki* occurrence of albitic jadeite is an exception to the Si-on-M1 rule for beam stability. We conclude that there must be additional factors governing behavior under the electron beam, but we do not yet have enough distinct cases to identify those additional factors. Possibilities include the effects of cation composition, site-ordering, or crystallite size.

Solid-state transformation versus crystallization from a melt

The formation of jadeite requires higher pressure than is found under static conditions anywhere in a chondritic parent body; the boundary of the reaction albite ⇌ jadeite +

SiO_2 rises from 1.65 GPa at 600 °C to 3.2 GPa at 1200 °C, where it meets the liquidus (Holland 1980). Hence the occurrence of jadeite in a chondritic meteorite is considered *prima facie* evidence of an impact event strong enough to transiently cross into the high pressure field where jadeite can form. However, two categories of mechanisms have been proposed for the formation of jadeite: solid-state transformation and crystallization from a melt (Ohtani et al. 2017). Solid-state transformation is indicated when jadeite occurrences display one or more of the following textural features: 1) lamellar intergrowth with another phase such as lingunite, 2) coexistence with particle-like or stringer-like amorphous silica, 3) pseudomorphs after albite. We note that these textural categories may depend on the scale of observation; in the L6 ordinary chondrite Yamato 74445, for example, lamellar intergrowth of jadeite with lingunite is visible at 2,000× magnification and, in addition, inclusions of particle-like amorphous silica become apparent at 10,000× magnification[30]. In contrast, jadeite growth from melt has been inferred from dendritic or spherulite-like textures. The dendritic development in Chelyabinsk includes needle-like and skeletal-rhombic crystals within feldspathic glass. The needles in particular are thought to have grown rapidly into feldspathic melt from nucleation sites on surfaces (Ozawa et al. 2014). The radial-concentric spherulite-like jadeite crystals in Novosibirsk, accompanied by chemical segregation of Na from K, are also inferred to indicate rapid crystallization from a melt (Bazhan et al. 2017a; Ozawa et al. 2014). Furthermore, in both Chelyabinsk and Novosibirsk, jadeite is found without any coexisting silica-rich phase (such as coesite, stishovite or glass), which is by itself strong evidence against any solid-state transformation from feldspar. On the other hand, for albitic jadeite we cannot use the absence of a coexisting silica phase as

409 evidence against solid-state transformation because at least some of the excess SiO_2
410 from the parent albite remains in the structure of this pyroxene.

411 In our observations of albitic jadeite, we find evidence for both solid-state
412 transformation and crystallization from melt. In *Ozerki*, we have indications for both
413 mechanisms within the same section: solid-state transformation is suggested by
414 particle-like texture (Fig. 1A) and poly-crystalline aggregates, whereas crystallization
415 from melt is suggested by spherulite-like crystals in the interior of melt pools (Fig.
416 1B), with fine-grained dendritic crystallites at the rim of glassy pools (Figs. 1C, D, H)
417 and skeletal hopper crystals (Fig. 1G). In *Chug Chug 011*, we see only dendritic
418 texture, suggesting crystallization from a melt (Figs. 2A, B). In *Chantonnay*, the
419 jadeite phase shows textures indicative of solid-state transformation: a lamellar
420 texture at low magnification that resolves to small particles at higher magnification
421 (Figs. 2C, 2D, 7).

422

423 **Risk of misidentified phases**

424 Before attempting to use the presence of a HP mineral to estimate *P-T* conditions in a
425 shock-metamorphosed specimen, such a phase must be thoroughly characterized and
426 its phase identification confirmed by the combination of one or more structure-
427 sensitive analytical methods (such as Raman spectroscopy, EBSD, XRD, or TEM)
428 and co-located compositional microanalysis (e.g., by EPMA). *P-T* inferences without
429 such information could be in error either because the phase is misidentified or because
430 its formation conditions depend on composition and may only have been
431 experimentally calibrated for a particular end member.

432 We catalogued a total of 19 documented occurrences of jadeite and its
433 relatives in ordinary chondrites (Table 1). These data include 13 type L6 meteorites,

two type L5, and one each of types LL5, LL7, H5/6, and H6. Most of these reports combine Raman data with near-albite compositional analyses. Only in four meteorites (Château-Renard, NWA 8275, Villalbeto de la Peña, Yamato 791384; references in Table 1) has the mineral structure been verified by TEM. Most published reports do not provide documentation whether the pyroxene phase coexists with a silica phase. Only one study documents jadeite coexisting with coesite (NWA 8257; Miyahara et al. 2017). At least one published study has foregone compositional analysis and relied on Raman spectra alone. The danger of such an inference was already shown by the presence of omphacite in the L6 Château-Renard (Baziotis et al. 2018) with a Raman spectrum indistinguishable from jadeite. In such a case, an analysis showing near-albite composition can rule out omphacite, but the Château-Renard observation shows that Raman spectra may not uniquely distinguish jadeite from other sodic pyroxenes with formation conditions different from those of pure jadeite.

The albitic jadeite in *Ozerki* and *Chug Chug 011*, both L6 chondrites, exhibits similar textures (mostly indicating crystallization from melt), yet *Ozerki* is classified as shock S4/5 (based on undulatory extinction, planar microstructures, and shocked melt veins) whereas *Chug Chug 011* has been classified as S2. We dispute the accepted classification of shock stage *Chug Chug 011*, given our observations of mosaicism in olivine and various shock-related melt veins, including one containing albitic jadeite. The investigated thin section of *Chug Chug 011* shows features more consistent with shock stage of at least S4. It remains to be determined, then, what shock pressure is implied by this mineral and its textural characteristics.

P-*T*-*t* histories

Shock-related melt veins (MVs) are generally thought to indicate local temperatures exceeding the liquidus of the matrix material, either under pressure or upon shock

459 pressure release (Langenhorst 2002). If the MV furthermore contains HP phases that
460 grew from a melt, one may further infer that peak conditions were above the liquidus
461 at HP and cooled enough for nucleation and growth of new phases to occur before
462 pressure release. In such a case, constraints on the cooling time of a MV translate
463 directly into a minimum time for the duration of the high-pressure pulse and hence the
464 characteristics of the impact event. On the other hand, the interpretation of HP phases
465 with textures indicative of solid-state transformation despite being found within melt
466 veins is more ambiguous. In the Ozerki section, albitic jadeite with texture suggesting
467 crystallization from the melt was found in the middle of MVs up to ~300 μm wide.
468 Although it is an unsolved problem to compute a precise cooling time for a shock
469 melt vein because of complexities such as turbulent mixing, an upper bound on
470 cooling time may be obtained from the simple cooling model of Turcotte & Schubert
471 (2014) and Langenhorst & Poirier (2000). Any turbulent transport will accelerate the
472 thermal equilibration of the hot melt vein with its cold surroundings and yield a
473 shorter time window for mineral growth. This upper bound time estimate for a 300
474 μm wide slab to cool from super-liquidus temperatures (~2000 °C) while surrounded
475 by cool matrix (~100 °C) is ~6.5 ms, using typical rock thermal diffusivity values.
476 Concerning pressure, albitic jadeite is less dense than lingunite and is expected
477 to form from an albite precursor at lower pressure. The absence of lingunite in the
478 studied meteorite sections suggests maximum pressure below 21 GPa, the minimum
479 pressure required for the formation of lingunite (Liu and El Goresy 2007). Other
480 bounds on pressure are traditionally based on experimental data involving stable,
481 stoichiometric pyroxenes coexisting with certain phase assemblages. For example, the
482 experiments of Bobrov et al. (2018) show that a pyroxene of composition $Jd_{70}Di_{30}$
483 begins to exsolve majorite garnet and stishovite above 13.5 GPa. Delay in nucleation

of garnet and stishovite might in fact weaken the 13.5 GPa constraint (Kubo et al. 2010) but, more importantly, the static experiments do not address either the upper or lower pressure limits for the metastable formation of albitic jadeite. Hence the albitic jadeite itself does not add any robust constraint to the pressure history at this time. Static equilibrium experiments at known *P* and *T* have so far not formed albitic jadeite as far as we are aware. As a general matter, lowering of the activity of jadeite component by the addition of albite and Ca-eskolaite components should expand the boundaries of the pyroxene liquidus field and allow growth over a larger pressure range than that for stoichiometric jadeite. To quantify this expansion and reveal the actual conditions for formation of albitic jadeite, however, it will be necessary to calibrate the shock pressures through a combination of dynamic experiments, *ab initio* and thermodynamic calculations, and observed coexistences with other pressure-sensitive indicator minerals and assemblages.

IMPLICATIONS

We report on three new occurrences of the recently described pyroxene species known as albitic jadeite (Ma et al. 2021) in the L6 chondrites *Ozerki*, *Chug Chug 011*, and *Chantonnay*. Each new occurrence was characterized by high-resolution SEM imaging, EDS and WDS compositional analysis, EBSD, and Raman spectroscopy. In addition, the *Chantonnay* material was further studied by FIB-TEM (Fig. 7). Like the omphacite in Château-Renard (Baziotis et al. 2018), all three new examples of albitic jadeite display Raman spectra that could be considered indicative of jadeite, yet each differs significantly from jadeite in their chemical composition. We define an enlarged compositional space defined by the end-members jadeite – kushiroite – supersilicic pyroxene that also includes notable molecules such as Ca-eskolaite, albite, and anorthite. Our triangular space has two major advantages: 1) it extends the Si

509 content to lower values than those of Ca-eskolaite and (2) it allows tissintite
510 compositions to be plotted in the same triangle as jadeite and albitic jadeite.

511 Furthermore, our results indicate that most but not all albitic jadeite is beam-
512 sensitive and, unlike true jadeite, rapidly becomes amorphous during EBSD analysis
513 and loses Na during TEM-EDS analysis. To substantiate the extent to which Raman
514 spectra can differentiate among jadeite and related species, at least under ideal
515 conditions, we used density functional theory and a model for thermal effects to
516 compute the 300 K Raman spectra of *C2/c* clinopyroxenes with the compositions
517 jadeite (Jd), albite (Ab), $Jd_{50}Ab_{50}$, tissintite, kushiroite, and silica. While the computed
518 spectra do show systematic differences, they are subtle enough to suggest that natural
519 specimens can only be distinguished under ideal analytical conditions.

520 Textural evidence shows that albitic jadeite may form both by crystallization
521 from a melt and by subsolidus transformation; in the case of *Ozerki,* both mechanisms
522 were seen within the same thin section.

523 At present, there is no sound basis for quantifying the difference in pressure
524 between the synthesis conditions of jadeite and albitic jadeite or the rate of change of
525 the boundary pressure as a function of excess Si content. Quantifying this will require
526 either experimental calibration, a detailed thermodynamic assessment or — most
527 likely — a judicious combination of static high-pressure experiments, shock recovery
528 experiments, and computational thermodynamics. Such an experimental and modeling
529 effort will potentially support development of a barometer that can translate
530 compositional and ordering parameters of these clinopyroxenes into a definite shock
531 pressure and time-temperature history. Such a barometer offers the advantages of
532 application to a wide range of meteorites (true jadeite being apparently quite rare).
533 However, it is possible that the experiments may fail if albitic jadeite lacks any

thermodynamic stability field and if shock recovery experiments are unable to match the shock durations required to grow and preserve the metastable phase.

We caution that formation conditions for albitic jadeite and other clinopyroxenes that share Raman bands with jadeite have not been characterized experimentally or fully cross-calibrated with other mineralogical indicators of shock conditions. Hence, to avoid possible errors (probably overestimates) in minimum pressure constraints based on the presence of jadeite, it is necessary to characterize any meteoritic occurrence with sufficient compositional and structural information to confirm that it is true, near-stoichiometric jadeite and not one of the related but distinct pyroxenes.

ACKNOWLEDGEMENTS

The authors are grateful to Dan Topa for assistance with the EPMA analyses. We thank an anonymous reviewer for helpful review comments. We gratefully recognize the efforts by the associate editor Oliver Tschauner for his constructive and fruitful review comments, and editorial handling. Ioannis Baziotis, Stamatios Xydous, and Angeliki Papoutsa received support for this research from ESF and the Greek State (call code EDBM103). Ioannis Baziotis thanks SYNTHESYS project AT-TAF-30 (www.synthesys.info; a European Union-funded Integrated Activities grant), which provided travel, accommodation, and instrument costs while using SEM and EPMA instruments at NHMV. Stamatios Xydous greatly thanks the Barringer Family Fund for Meteorite Impact Research for its support. Analyses at Caltech were funded by NASA award 80NSSC18K0532. Razvan Caracas acknowledges support from the European Research Council under EU Horizon 2020 research and innovation program (grant agreement 681818 – IMPACT), the Research Council of Norway, project

558 number 223272, and access to supercomputing facilities via eDARI stl2816 grants,
559 PRACE RA4947 grant, and Uninet2 NN9697K grant.

560

561

562 **REFERENCES CITED**

563 Acosta-Maeda, T., Scott, E., Sharma, S., and Misra, A. (2013) The pressures and
564 temperatures of meteorite impact: Evidence from micro-Raman mapping of
565 mineral phases in the strongly shocked Taiban ordinary chondrite. American
566 Mineralogist 98, 859-869.

567 Baroni, S., de Gironcoli, S., Dal Corso, A., and Giannozzi, P. (2001) Phonons and
568 related crystal properties from density-functional perturbation theory. Reviews
569 of modern Physics 73, 515–562.

570 Bazhan, I., Ozawa, S., Miyahara, M., Ohtani, E., and Litasov, K. (2017a) "Spherulite-
571 like" jadeite growth in shock-melt veins of the Novosibirsk H5/6 chondrite.
572 Russian Geology and Geophysics 58, 12-19.

573 Bazhan, I., Litasov, K., Ohtani, E., and Ozawa, S. (2017b) Majorite-olivine–high-Ca
574 pyroxene assemblage in the shock-melt veins of Pervomaisky L6 chondrite.
575 American Mineralogist: Journal of Earth and Planetary Materials 102, 1279-
576 1286.

577 Baziotis, I. P., Liu, Y., DeCarli, P. S., Melosh, H. J., McSween, H. Y., Bodnar, R. J.,
578 and Taylor, L. A. (2013) The Tissint Martian meteorite as evidence for the
579 largest impact excavation. Nature Communications 4, 1-7.

580 Baziotis, I., Asimow, P., Hu, J., Ferrière, L., Ma, C., Cernok, A., Anand, M., and
581 Topa, D. (2018) High pressure minerals in the Château-Renard (L6) ordinary
582 chondrite: implications for collisions on its parent body. Scientific Reports 8,
583 1-16.

584 Bobrov, A., Kojitani, H., Akaogi, M., and Litvin, Y. (2008) Phase relations on the
585 diopside–jadeite–hedenbergite join up to 24 GPa and stability of Na-bearing
586 majoritic garnet. Geochimica et Cosmochimica Acta 72, 2392-2408.

587 Caracas, R., and Cohen, R. E. (2006) Theoretical determination of the Raman spectra
588 of $MgSiO_3$ perovskite and post-perovskite at high pressure. Geophysical
589 Research Letters 33.
590 Caracas, R., and Bobocioiu, E. (2011) The WURM project—a freely available web-
591 based repository of computed physical data for minerals. American
592 Mineralogist 96, 437-443.
593 Černok, A., Marquardt, K., Caracas, R., Bykova, E., Habler, G., Liermann, H. P., Hanfland,
594 M., Mezouar, M., Bobocioiu, E. and Dubrovinsky, L. (2017) Compressional
595 pathways of α-cristobalite, structure of cristobalite XI, and towards the understanding
596 of seifertite formation. Nature Communications 8, 1-10.
597 Dodd, R., and Jarosewich, E. (1982a) The compositions of incipient shock melts in L6
598 chondrites. Earth and Planetary Science Letters 59, 355-363.
599 Dodd, R., Jarosewich, E., and Hill, B. (1982b) Petrogenesis of complex veins in the
600 Chantonnay (L6f) chondrite. Earth and Planetary Science Letters 59, 364-374.
601 Feng, L., Miyahara, M., Nagase, T., Ohtani, E., Hu, S., El Goresy, A., and Lin, Y.
602 (2017) Shock-induced PT conditions and formation mechanism of akimotoite-
603 pyroxene glass assemblages in the Grove Mountains (GRV) 052082 (L6)
604 meteorite. American Mineralogist 102, 1254-1262.
605 Friedrich, J., Bridges, J., Wang, M.-S., and Lipschutz, M. (2004) Chemical studies of
606 L chondrites. VI: Variations with petrographic type and shock-loading among
607 equilibrated falls. Geochimica et Cosmochimica Acta 68, 2889-2904.
608 Gillet, P., Chen, M., Dubrovinsky, L., and El Goresy, A. (2000) Natural $NaAlSi_3O_8$-
609 hollandite in the shocked Sixiangkou meteorite. Science 287, 1633-1636.
610 Gonze, X., Rignanese, G. M., and Caracas, R. (2005) First-principle studies of the
611 lattice dynamics of crystals, and related properties. Zeitschrift für
612 Kristallographie-Crystalline Materials 220, 458-472.

613 Gonze, X., Amadon, B., Anglade, P.-M., Beuken, J.-M., Bottin, F., Boulanger, P.,
614 Bruneval, F., Caliste, D., Caracas, R., Côté, M., and others (2009) ABINIT:
615 First-principles approach to material and nanosystem properties. Computer
616 Physics Communications 180, 2582–2615.
617 Holland, T. (1980) The reaction albite = jadeite + quartz determined experimentally in
618 the range 600–1200 C. American Mineralogist 65, 129-134.
619 Imae, N., and Ikeda, Y. (2010) High-pressure polymorphs of magnesian
620 orthopyroxene from a shock vein in the Yamato-000047 lherzolitic
621 shergottite. Meteoritics and Planetary Science 45, 43-54.
622 James, O. (1969) Jadeite: shock-induced formation from oligoclase, Ries Crater,
623 Germany. Science 165, 1005-1008.
624 Kimura, M., Suzuki, A., Ohtani, E., and El Goresy, A. (2001) Raman petrography of
625 high-pressure minerals in H, L, LL and E-chondrites. Meteoritics and
626 Planetary Science Supplement 36, A99.
627 Kubo, T., Kimura, M., Kato, T., Nishi, M., Tominaga, A., Kikegawa, T., and
628 Funakoshi, K.-I. (2010) Plagioclase breakdown as an indicator for shock
629 conditions of meteorites. Nature Geosciences 3, 41-45.
630 Kubo, T., Kato, T., Higo, Y., and Funakoshi, K.-I. (2015) Curious kinetic behavior in
631 silica polymorphs solves seifertite puzzle in shocked meteorite. Science
632 Advances 1, e1500075.
633 Kubo, T., Kono, M., Imamura, M., Kato, T., Uehara, S., Kondo, T., Higo, Y., Tange,
634 Y. and Kikegawa, T. (2017) Formation of a metastable hollandite phase from
635 amorphous plagioclase: A possible origin of lingunite in shocked chondritic
636 meteorites. Physics of the Earth and Planetary Interiors 272, 50-57.

637 Lafuente B., Downs R. T., Yang H., and Stone N. (2015) 1. The power of databases:
638 The RRUFF project. In Highlights in Mineralogical Crystallography, edited by
639 Armbruster T. and Danisi R.M. Berlin/Munich/Boston: De Gruyter. pp. 1–30,
640 https://doi.org/10.1515/9783110417104-003.
641 Langenhorst, F. (2002) Shock metamorphism of some minerals: Basic introduction
642 and microstructural observations. Bulletin of the Czech Geological Survey 77,
643 265-282.
644 Litasov, K., and Badyukov, D. (2019) Raman Spectroscopy of High-Pressure Phases
645 in Shocked L6 Chondrite NWA 5011. Geochemistry International 57, 912-
646 922.
647 Liu, L.-G. (1978) High-pressure phase transformations of albite, jadeite and
648 nepheline. Earth and Planetary Science Letters 37, 438-444.
649 Liu, L.-G., and El Goresy, A. (2007) High-pressure phase transitions of the feldspars,
650 and further characterization of lingunite. International Geology Review 49,
651 854-860.
652 Ma, C., Tschauner, O., Beckett, J., Liu, Y., Rossman, G., Zhuravlev, K., Prakapenka,
653 V., Dera. P. and Taylor, L. (2015) Tissintite, (Ca, Na, □)$AlSi_2O_6$, a highly-
654 defective, shock-induced, high-pressure clinopyroxene in the Tissint martian
655 meteorite. Earth and Planetary Science Letters 422, 194-205.
656 Ma, C., Tschauner, O., Kong, M., Beckett, J. R., Greenberg, E., Prakapenka, V. B.,
657 and Lee, Y. (2021) A high-pressure, clinopyroxene-structured polymorph of
658 albite in highly shocked terrestrial and meteoritic rocks. American
659 Mineralogist, in press. DOI:10.2138/am-2021-7925.
660 Martinez, M., Brearley, A., Trigo-Rodríguez, J., and Llorca, J. (2019) New
661 observations on high-pressure phases in a shock melt vein in the Villalbeto de

662 la Peña meteorite: Insights into the shock behavior of diopside. Meteoritics
663 and Planetary Science 54, 2845-2863.
664 Miyahara, M., Ozawa, S., Ohtani, E., Kimura, M., Kubo, T., Sakai, T., Nagase, T.,
665 Nishijima, M. and Hirao, N. (2013) Jadeite formation in shocked ordinary
666 chondrites. Earth and Planetary Science Letters 373, 102-108.
667 Miyahara, M., El Goresy, A., Ohtani, E., Nagase, T., Nishijima, M., Vashaei, Z.,
668 Ferroir, T., Gillet, P., Dubrovinsky, L. and Simionovici, A. (2008) Evidence
669 for fractional crystallization of wadsleyite and ringwoodite from olivine melts
670 in chondrules entrained in shock-melt veins. Proceedings of the National
671 Academy of Sciences 105, 8542-8547.
672 Miyahara, M., Ohtani, E., and Yamaguchi, A. (2017) Albite dissociation reaction in
673 the Northwest Africa 8275 shocked LL chondrite and implications for its
674 impact history. Geochimica et Cosmochimica Acta 217, 320-333.
675 Monkhorst, H.J., and Pack, J.D. (1976) Special points for Brillouin-zone integrations.
676 Physical review B 13, 5188–5192.
677 Ohtani, E., Kimura, Y., Kimura, M., Takata, T., Kondo, T., and Kubo, T. (2004)
678 Formation of high-pressure minerals in shocked L6 chondrite Yamato 791384:
679 constraints on shock conditions and parent body size. Earth and Planetary
680 Science Letters 227, 505-515.
681 Ohtani, E., Kimura, Y., Kimura, M., Kubo, T., and Takata, T. (2006) High-pressure
682 minerals in shocked L6-chondrites: constraints on impact conditions. Shock
683 Waves 16, 45-52.
684 Ohtani, E., Ozawa, S., and Miyahara, M. (2017) Jadeite in shocked meteorites and its
685 textural variations. Journal of Mineralogical and Petrological Sciences
686 170329.

687 Ozawa, S., Ohtani, E., Miyahara, M., Suzuki, A., Kimura, M., and Ito, Y. (2009)
688 Transformation textures, mechanisms of formation of high-pressure minerals
689 in shock melt veins of L6 chondrites, and pressure-temperature conditions of
690 the shock events. Meteoritics and Planetary Science 44, 1771-1786.
691 Ozawa, S., Miyahara, M., Ohtani, E., Koroleva, O., Ito, Y., Litasov, K., and
692 Pokhilenko, N. (2014) Jadeite in Chelyabinsk meteorite and the nature of an
693 impact event on its parent body. Scientific Reports 4, 5033.
694 Pang, R.-L., Zhang, A.-C., Wang, S.-Z., Wang, R.-C., and Yurimoto, H. (2016) High-
695 pressure minerals in eucrite suggest a small source crater on Vesta. Sciemtific
696 Reports 6, 26063.
697 Payne, M.C., Teter, M.P., Allan, D.C., Arias, T.A., and Joannopoulos, J.D. (1992)
698 Iterative minimization techniques for ab initio total-energy calculations:
699 Molecular dynamics and conjugate gradients. Reviews of modern Physics 64,
700 1045–1097.
701 Prencipe, M. (2012) Simulation of vibrational spectra of crystals by ab initio
702 calculations: an invaluable aid in the assignment and interpretation of the
703 Raman signals. The case of jadeite ($NaAlSi_2O_6$). Journal of Raman
704 Spectroscopy 43, 1567-1569.
705 Prencipe, M., Maschio, L., Kirtman, B., Salustro, S., Erba, A., and Dovesi, R. (2014)
706 Raman spectrum of $NaAlSi_2O_6$ jadeite. A quantum mechanical simulation.
707 Journal of Raman Spectroscopy 45, 703-709.
708 Rucks, M., Whitaker, M., Glotch, T., Parise, J., Jaret, S., Catalano, T., and Dyar, M.
709 (2018) Making tissintite: Mimicking meteorites in the multi-anvil. American
710 Mineralogist: Journal of Earth and Planetary Materials 103, 1516-1519.

Sharp, T., Xie, Z., de Carli, P., and Hu, J. (2015) A large shock vein in L chondrite Roosevelt County 106: Evidence for a long-duration shock pulse on the L chondrite parent body. Meteoritics and Planetary Science 50, 1941-1953.

Smith, D. (1984) Coesite in clinopyroxene in the Caledonides and its implications for geodynamics. Nature 310, 641-644.

Tschauner, O., Ma, C., Beckett, J., Prescher, C., Prakapenka, V., and Rossman, G. (2014) Discovery of bridgmanite, the most abundant mineral in Earth, in a shocked meteorite. Science 346, 1100-1102.

Veithen, M., Gonze, X., and Ghosez, Ph. (2005) Non-linear optical susceptibilities, Raman efficiencies and electrooptic tensors from first-principles density functional perturbation theory. Physical review B 71, 125107.

Yagi, A., Suzuki, T., and Akaogi, M. (1994) High pressure transitions in the system $KAlSi_3O_8$-$NaAlSi_3O_8$. Physics and Chemistry of Minerals 21, 12-17.

Yang, H., Konzett, J., Frost, D., and Downs, R. (2009) X-ray diffraction and Raman spectroscopic study of clinopyroxenes with six-coordinated Si in the Na $(Mg_{0.5}Si_{0.5})Si_2O_6$-$NaAlSi_2O_6$ system. American Mineralogist 94, 942-949.

Zhang, A., Hsu, W., Wang, R., and Ding, M. (2006) Pyroxene polymorphs in melt veins of the heavily shocked Sixiangkou L6 chondrite. European Journal of Mineralogy 18, 719-726.

Figure captions

Fig. 1 Back-scattered electron (BSE) images of occurrences of albitic jadeite in *Ozerki*. The images display textures indicative of both solid-state transformation (A) and crystallization from melt (B-F). A) Particle-like texture of amorphous material mixed with albitic jadeite. B) Spherulite-like crystals at the rim of a glassy melt pool. (C, D) Dendritic crystals showing a characteristic zonation inward from the melt-vein boundary. (E, F, G) High-resolution images of skeletal-hopper and (H) dendritic crystals inside a melt pocket.

Fig. 2 BSE images showing textural features of albitic jadeite in *Chug Chug 011* (A, B) and *Chantonnay* (C, D). (A) 12,000× view with locations of co-located Raman spots indicated. (B) 40,000× view of dendritic growth pattern. (C) BSE image of a melt vein in *Chantonnay*, with a melt pool at the center. (D) Enlargement of the melt pool within melt vein matrix. White circle denotes a Raman spot (spectrum A_HP03_bright area" in Fig. 4D). The dashed box marks the location of the extracted FIB section (see Figure 7).

Fig. 3 The silipyx [Spx; $(\square)^{M2}(Si)^{M1}(Si_2)^{T}O_6$] – jadeite [Jd; $(Na)^{M2}(Al)^{M1}(Si_2)^{T}O_6$)] – kushiroite [Ku; $(Ca)^{M2}(Al)^{M1}(AlSi)^{T}O_6$)] diagram, showing notable compositional end-members albite (Ab), Ca-eskolaite (Ca-Esk), and anorthite (An), as well as jadeite, tissintite, and albitic jadeite analyses from the literature (Ma et al. 2020, 2021; Bazhan et al. 2017a; Ozawa et al. 2014; Miyahara et al. 2017; Baziotis et al. 2018; Bazhan et al. 2017b; Martinez et al. 2019; Miyahara et al. 2013; Ohtani et al. 2006; Ozawa et al. 2009; Zhang et al. 2006) and from this work. Dashed contours indicate atoms of Si per 6 O formula unit (black) and vacancies per formula unit (grey). A) Published data. (B) This work. In (B), the open symbols correspond to *Chantonnay* analyses showing the effect of Na loss, which affects some beam-sensitive albitic jadeites.

Fig. 4 Measured (A) and calculated (B-G) Raman spectra. All spectra are normalized to common maximum intensity and offset for clarity. A) Raman peaks at ~376, 698, 986, and ~1036 cm^{-1} are typical for jadeite (Jd; reference spectrum R050220 from RRUFF database shown). The high-wavenumber range of Tissintite (Tis) spectra, by contrast, has a single broad peak centered at ~1000 cm^{-1} (Ma et al. 2015). Spectra in *Ozerki* have all four main Raman peaks. In *Chug Chug 011* (CC), numerous spectra display the peak at 698 cm^{-1} associated with jadeite, however the 376 cm^{-1} peak of jadeite is shifted to ~388 cm^{-1} and the two high-wavenumber peaks are not resolved. In one CC spectrum, the peak at 960 cm^{-1} indicates an apatite inclusion. In *Chantonnay* (Ch), the peaks in at ~204,

222, 254, 377, 699, 987, and 1038 cm^{-1} are all near-ideal matches for jadeite. The calculated Raman spectra are for (B) kushiroite [$(Ca)^{M1}(Al)^{M2}(Al,Si)^{T}O_6$], (C) tissintite [$(Ca_{0.75}\square_{0.25})^{M1}(Al)^{M2}(Al,Si)^{T}O_6$], (D) jadeite [$(Na)^{M1}(Al)^{M2}(Si_2)^{T}O_6$], (E) intermediate [$(Na_{0.875}\square_{0.125})^{M1}(Al_{0.875}Si_{0.125})^{M2}(Si_2)^{T}O_6$], (F) albitic jadeite [$(Na_{0.75}\square_{0.25})^{M1}(Al_{0.75}Si_{0.25})^{M2}(Si_2)^{T}O_6$], and (G) silipyx [$(\square)^{M1}(Si)^{M2}(Si_2)^{T}O_6$]. The computed spectra are represented as delta functions. The solid black line corresponds to an artificial Gaussian broadening of the peaks with an arbitrary FWHM of 25 cm^{-1}, to facilitate comparison to the experimental spectra.

Fig. 5 Raman mapping of feldspathic pool in *Ozerki* (A-C) and *Chug Chug 011* (D-E). A) BSE image of the feldspathic pool, showing elongated and equant crystals at the edge and interior of the pool, respectively. B) Raman map (of the boxed area in the SEM image) superposed on reflected light image in greyscale. Red and blue color represent the intensity of diagnostic peaks of 'jadeite' and diopside, respectively. Purple color at the edge of the pool indicates coexistence of the two peaks. C) Representative Raman spectrum from the purple area. No Raman signature of polymorphs of silica is observed in this area. D) BSE image of *Chug Chug 011* with mapped area indicated by white square. E) Raman maps of intensity of diopside peak in blue and 'jadeite' peak in red. Grey background indicates no strong fluorescence with no diagnostic peaks, corresponding to feldspathic glass.

Fig. 6 Electron backscatter diffraction (EBSD) patterns. Albitic jadeite from (A, B) *Ozerki* and (C, D) *Chug Chug 011*, both indexed with a *C2/c* clinopyroxene structure. These materials were sufficiently beam-stable to collect a pattern.

Fig. 7 Transmission electron microscopy data. (A) A focused ion beam (FIB) section extracted from the boundary of the *Chantonnay* melt pool at the location indicated in figure 2D. (B) Bright field image of the Si-pool end of the FIB section. The homogeneous matrix is Si-rich glass. The grains with contrast to the matrix are fine clinopyroxene (cpx) crystals. The different apparent brightness of the grains results from different crystallographic orientations; the darkest grains are viewed nearly along a major zone axis. (C) Selected area electron diffraction (SAED) patterns for three of the dark crystals seen in (B), rotated to low-index zone axes. All the patterns indicate a *C2/c* clinopyroxene structure.

Table 1 Summary of the occurrences of jadeite and its relatives in ordinary chondrites

Meteorite	Type	Applied Method			Chemistry	Coexistence with SiO_2	Likely formation mechanism	Reference
		RS	EBSD	TEM				
ALH78003	L6	jd	n.a.	n.a.	EPMA: $Ca_{0.10}Na_{0.76}K_{0.04}Fe_{0.01}Al_{1.10}Si_{2.92}O_8$	n.o.	n.p.	Ohtani et al. (2006)
Chantonnay (this study)	L6	jd	ambiguous: *jd* or *Ca-px*	*C2/c*	SEM-EDS: $Ca_{0.05}Na_{0.42}Mg_{0.11}Al_{0.93}Si_{2.11}O_6$	n.o.	s.s.t.	
Château-Renard	L6	jd+Ca-px	ambiguous: *jd or omph*	*P2/n*	EPMA: $Ca_{0.07\text{-}0.10}Na_{0.25\text{-}0.46}Fe_{0.16\text{-}0.19}Mg_{0.35\text{-}1.12}Al_{0.29\text{-}0.57}Si_{2.01\text{-}2.04}O_6$	n.o.		Baziotis et al. (2018)
Chelyabinsk	LL5	jd+ol	n.a.	n.a.	SEM-EDS: $Ca_{0.10}Na_{0.72}K_{0.06}Fe_{0.03}Al_{1.07}Si_{2.93}O_8$	n.o.	c.f.m.	Ozawa et al. (2014)
Chug Chug 011 (this study)	L6	jd	n.a.	n.a.	SEM-EDS: $Ca_{0.07\text{-}0.15}Na_{0.49\text{-}0.64}K_{0.03\text{-}0.05}Fe_{0.00\text{-}0.13}Mg_{0.00\text{-}0.45}Al_{0.62\text{-}0.86}Si_{2.04\text{-}2.18}O_6$	n.o.		
GRV 052082	L6	jd (poor quality)	n.a.	n.a.	n.g.	n.o.	n.p.	Feng et al. (2017)
Novosibirsk	H5/6	jd+opx+ol/ jd+gl	n.a.	n.a.	SEM-EDS: $Ca_{0.09\text{-}0.12}Na_{0.64\text{-}0.68}K_{0.06\text{-}0.11}Fe_{0.04}Mg_{0.02}Al_{1.10}Si_{2.89\text{-}2.90}O_8$	n.o.	c.f.m.	Bazhan et al. (2017a)
NWA 8275	LL7	jd+coe/ jd+amo	n.a.	Consistent with jd and coe	EPMA: $Ca_{0.13}Na_{0.84}K_{0.02}Fe_{0.03}Al_{1.13}Si_{2.86}O_8$ (jd+coe) $Ca_{0.16}Na_{0.78}K_{0.02}Fe_{0.02}Al_{1.16}Si_{2.84}O_8$ (jd+amo) SEM-EDS: $Ca_{0.06}Na_{0.67}K_{0.02}Al_{0.92}Si_{2.11}O_6$	Coe	s.s.t. and c.f.m.	Miyahara et al. (2017
Ozerki (this study)	L6	jd	n.a.	n.a.	EPMA: $Ca_{0.07\text{-}0.08}Na_{0.48\text{-}0.62}K_{0.03\text{-}0.05}Fe_{0.01\text{-}0.06}Mg_{0.00\text{-}0.08}Al_{0.77\text{-}0.81}Si_{2.14\text{-}2.23}O_6$ EPMA-EDS: $Ca_{0.15}Na_{0.70}K_{0.05}Al_{0.82}Si_{2.10}O_6$	n.o.	c.f.m.	
Peace River	L6	+	+	+	+	gl	possible s.s.t.	Miyahara et al. (2008)
Pervomaisky	L6	jd+maj-prp+ol+Ca-px	n.a.	n.a.	SEM-EDS: $Ca_{0.11}Na_{0.81}K_{0.04}Fe_{0.06}Mg_{0.02}Al_{1.06}Si_{2.90}O_8$	n.o.	c.f.m.	Bazhan et al. (2017b)
Roosevelt Country 106	L6	jd+lin+fsp	n.a.	n.a.	n.g.	n.o.	n.p.	Sharp et al. (2015)
Sahara 98222	L6	jd	n.a.	n.a.	EPMA: $Ca_{0.10}Na_{0.83}K_{0.04}Fe_{0.02}Al_{1.11}Si_{2.89}O_8$ (jd+possible amo)	n.o.	s.s.t.	Ohtani et al. (2006)
Sixiangkou	L6	jd+maj	n.a.	n.a.	EPMA: $Ca_{0.10}Na_{0.14}K_{0.06}Fe_{0.03}Al_{1.12}Si_{3.04}O_8$	n.o.	n.p.	Zhang et al. (2006)
Taiban	L5	jd+maj/ jd+Ca-cpx	n.a.	n.a.	n.g.	n.o.	c.f.m.	Acosta-Maeda et al. (2013)
Villaibeto de la Peña	L6	mixture of jd+lin	n.a.	Consistent with lin	EPMA: $Ca_{0.12}Na_{0.63}K_{0.03}Fe_{0.01}Mg_{0.01}Mn_{0.01}Al_{1.18}Si_{2.87}O_8$	n.o.	possible s.s.t.	Martinez et al. (2019)
Y-75100		jd+mask	n.a.	n.a.	EPMA: $Ca_{0.09}Na_{0.80}K_{0.05}Fe_{0.03}Al_{1.11}Si_{2.87}O_8$ SEM-EDS: $Ca_{0.09}Na_{0.72\text{-}0.73}K_{0.02}Al_{0.94\text{-}0.96}Si_{2.06}O_6$	n.o.	s.s.t.	Miyahara et al. (2013)
Y-74445	L6	lin+jd*	n.a.	n.a.	EPMA: $Ca_{0.06}Na_{0.78}K_{0.02}Fe_{0.02}Al_{1.10}Si_{2.93}O_8$	n.o.	s.s.t.	Ozawa et al. (2009)
Y-791384	L6	jd	jd (*C2/c*)**	jd+amo	EPMA: $Ca_{0.09}Na_{0.80}K_{0.05}Fe_{0.03}Al_{0.40}Si_{2.90}O_8$ (Ab-jd) SEM-EDS: $Ca_{0.05\text{-}0.09}Na_{0.85\text{-}0.98}K_{0.00\text{-}0.02}Al_{0.87\text{-}0.95}Si_{2.02\text{-}2.06}O_6$	n.o.	s.s.t.	Miyahara et al. (2013); Ohtani et al. (2004, 2006)
Y-8410	LL5	+	+	+	+	+	n.p.	Kimura et al. (2001)
NWA 5011	L6	jd+maj	n.a.	n.a.	n.g.	n.o.	n.p.	Litasov and Badyukov (2019)

n.o.: not observed; n.a.: not applied; n.g.: not given; n.p.: not possible to infer because of absence of adequate images; s.s.t.: solid-state transformation; c.f.m.: crystallization from melt; RS: raman spectroscopy; EBSD: electron back-scatter diffraction; TEM: transmission electron microscopy.
Where more than one study reported jadeite and its relatives, we used the most recent one (citation number in bold). Abbreviations: jd: jadeite; omph: omphacite; maj-prp: majorite-pyrope; lin: lingunite; opx: orthopyroxene; Ca-px: high-Ca pyroxene; fsp: feldspar; coe: coesite; mask: maskelynite; gl: glass; amo: amorphous material. *: Ozawa et al. (Ozawa, et al., 2009) claim in the text (based on BSE images) the coexistence of lingunite+jadeite, however, their Raman spectrum (their fig.7f) shows the characteristic strong peak for lingunite only. **: applied method was synchrotron x-ray diffraction. + not sufficient data to justify jadeite structure and chemistry.

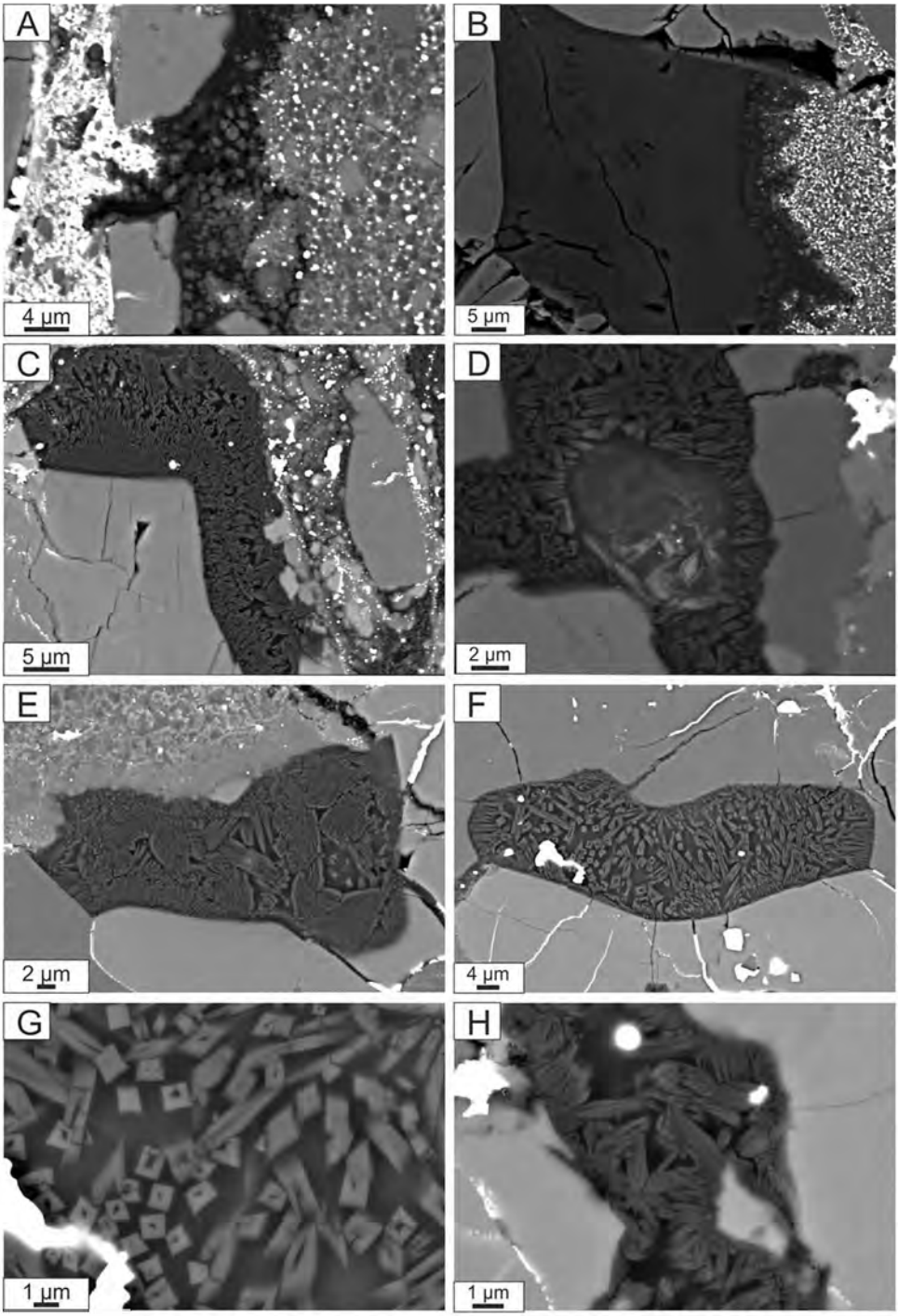

Figure 1

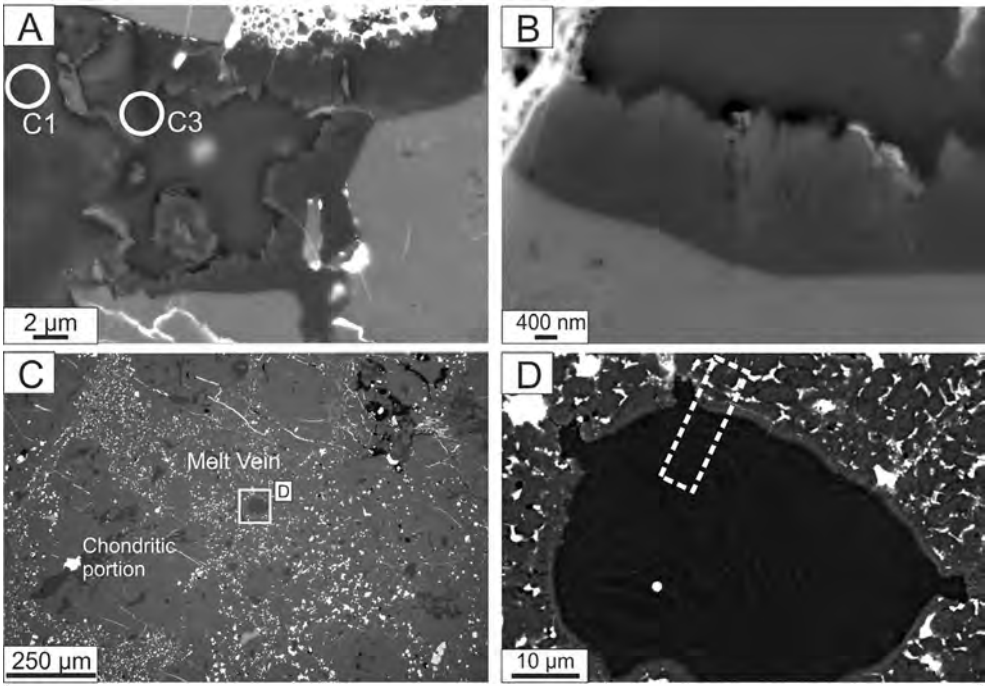
A
C1
C3
2 µm
B
400 nm
C
Melt Vein
D
Chondritic
portion
250 µm
D
10 µm

Figure 2

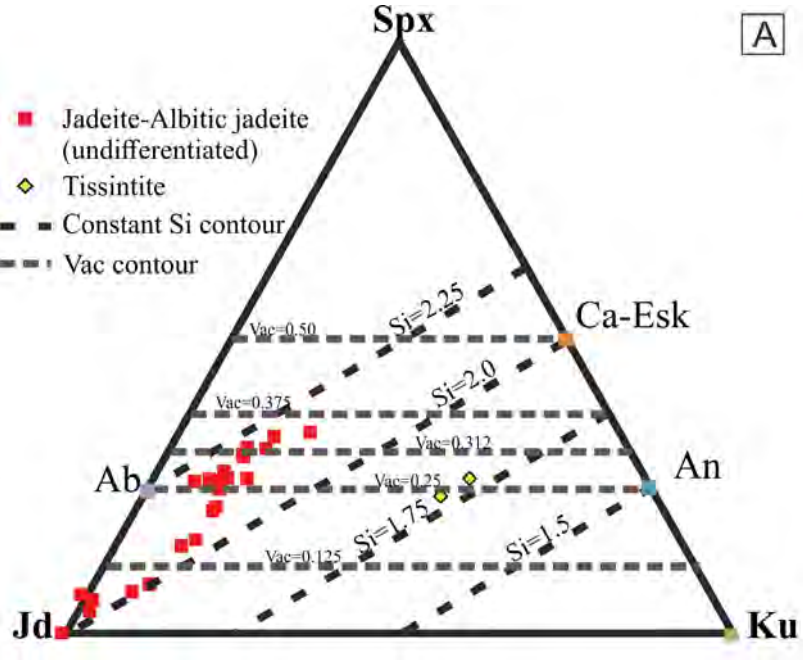
Spx
A
Jadeite-Albitic jadeite
(undifferentiated)
Tissintite
Constant Si contour
Vac contour
Vac=0.50
Si=2.25
Ca-Esk
Vac=0.375
Si=2.0
Vac=0.312
Ab
An
Vac=0.25
Si=1.75
Si=1.5
Vac=0.125
Jd
Ku

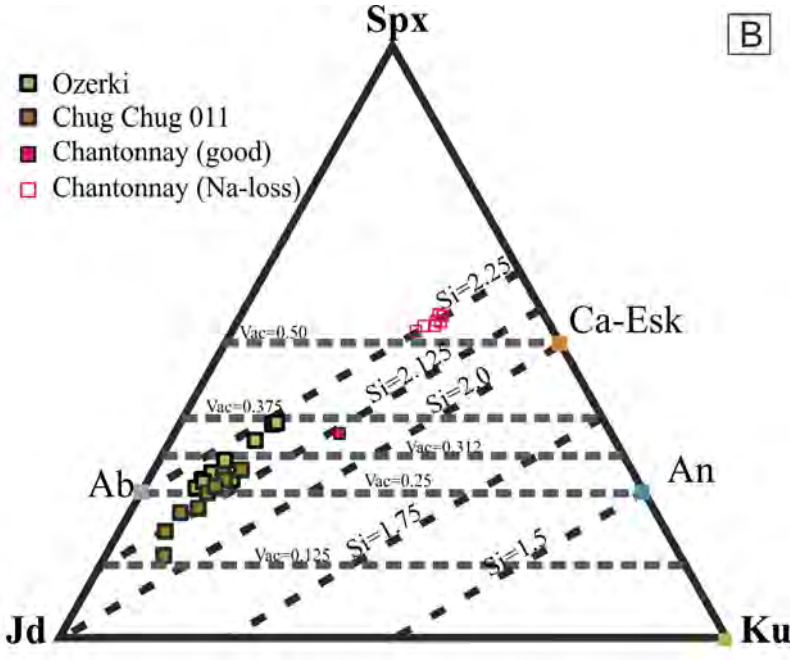
Spx
B
Ozerki
Chug Chug 011
Chantonnay (good)
Chantonnay (Na-loss)
Si=2.25
Vac=0.50
Ca-Esk
Si=2.125
Vac=0.375
Si=2.0
Vac=0.312
Ab
An
Vac=0.25
Si=1.75
Vac=0.125
Si=1.5
Jd
Ku

Figure 3

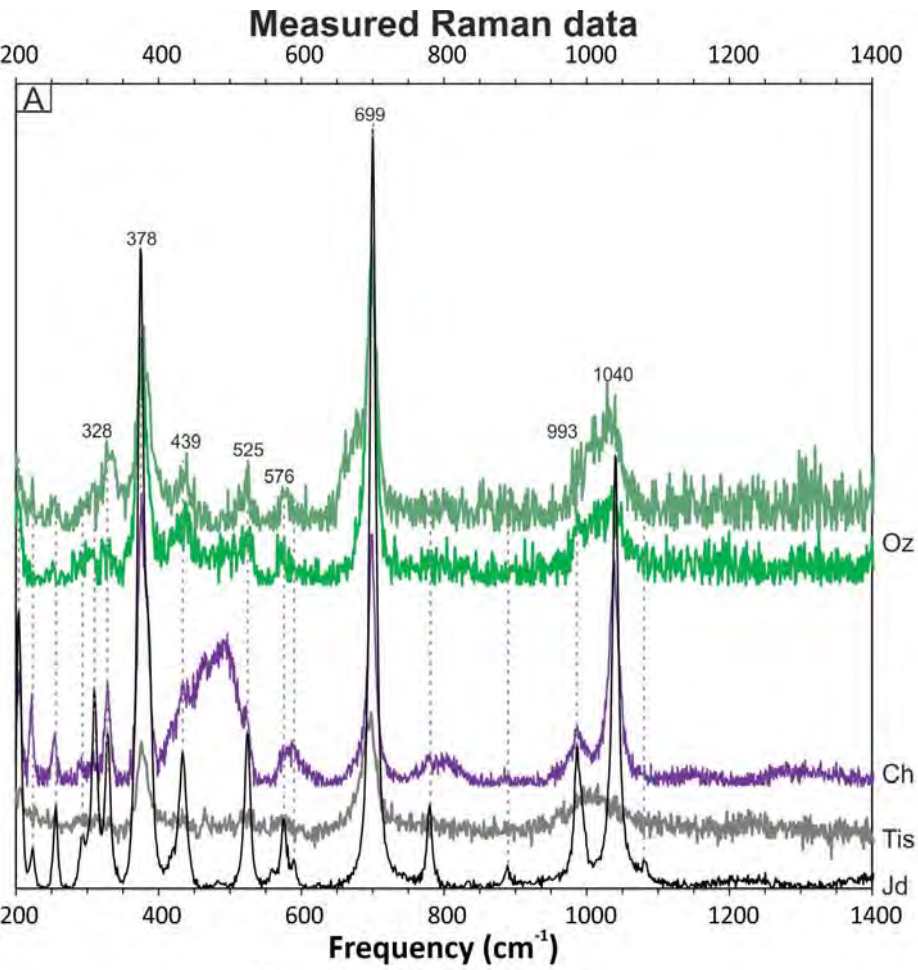
Measured Raman data
A
699
378
328
439
525
576
993
1040
Oz
Ch
Tis
Jd
Frequency (cm-1)

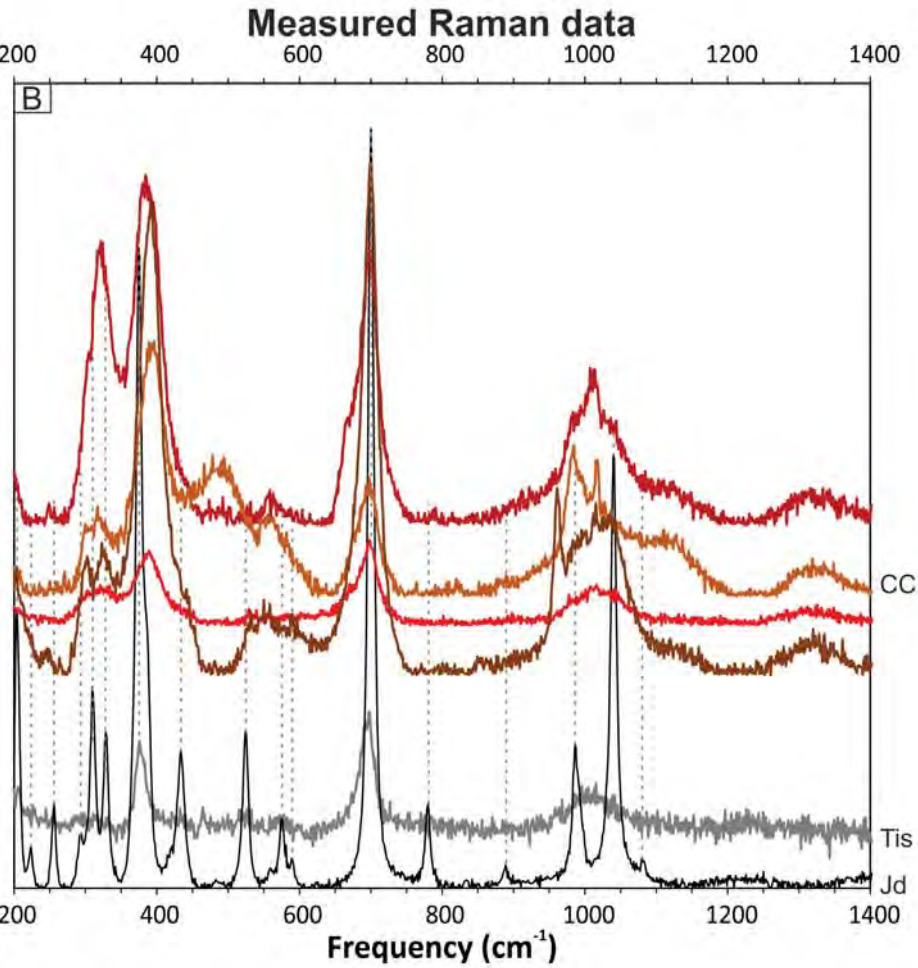
Measured Raman data
B
CC
Tis
Jd
Frequency (cm-1)

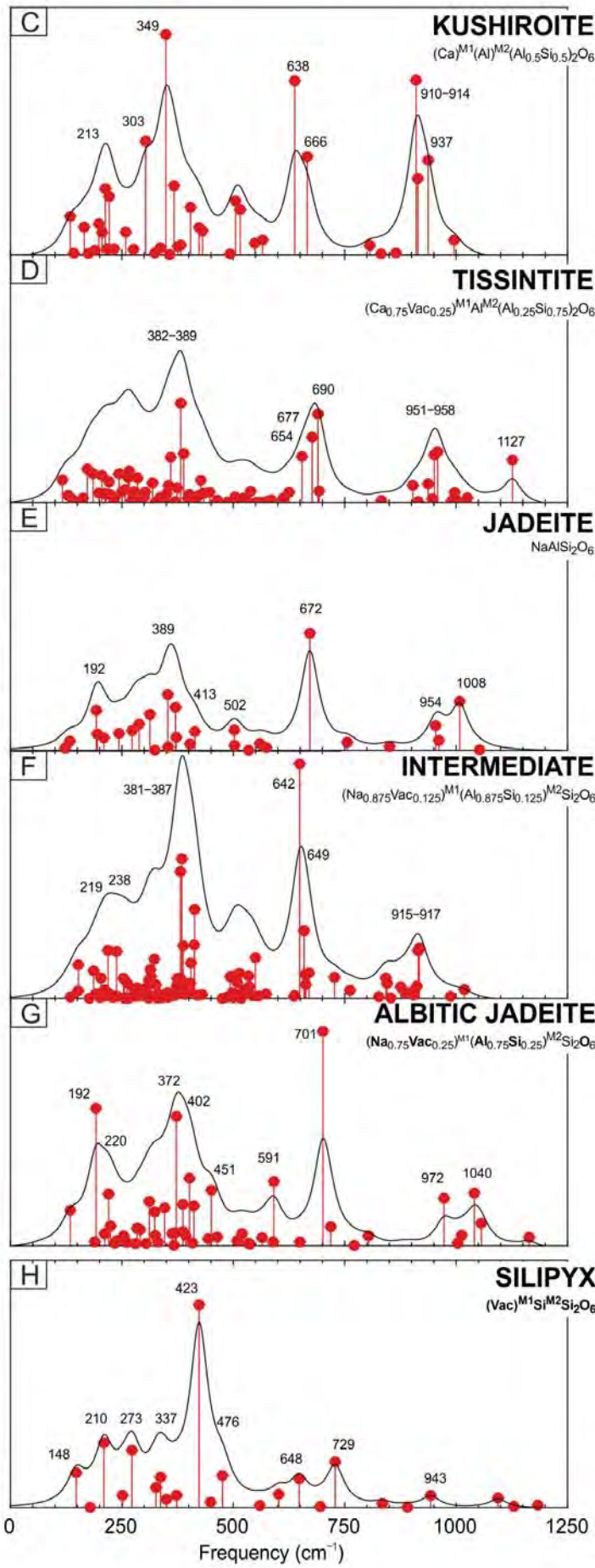
Calculated Raman spectra
C
KUSHIROITE
(Ca)M1(Al)M2(Al0.5Si0.5)2O6
349
638
910–914
213
303
666
937
D
TISSINTITE
(Ca0.75Vac0.25)M1AlM2(Al0.25Si0.75)2O6
382–389
690
677
654
951–958
1127
E
JADEITE
NaAlSi2O6
672
389
192
413
502
954
1008
F
INTERMEDIATE
(Na0.875Vac0.125)M1(Al0.875Si0.125)M2Si2O6
381–387
642
649
219
238
915–917
G
ALBITIC JADEITE
(Na0.75Vac0.25)M1(Al0.75Si0.25)M2Si2O6
701
372
192
402
220
451
591
972
1040
H
SILIPYX
(Vac)M1SiM2Si2O6
423
210
273
337
476
148
729
648
943
0
250
500
750
1000
1250
Frequency (cm-1)

Figure 4

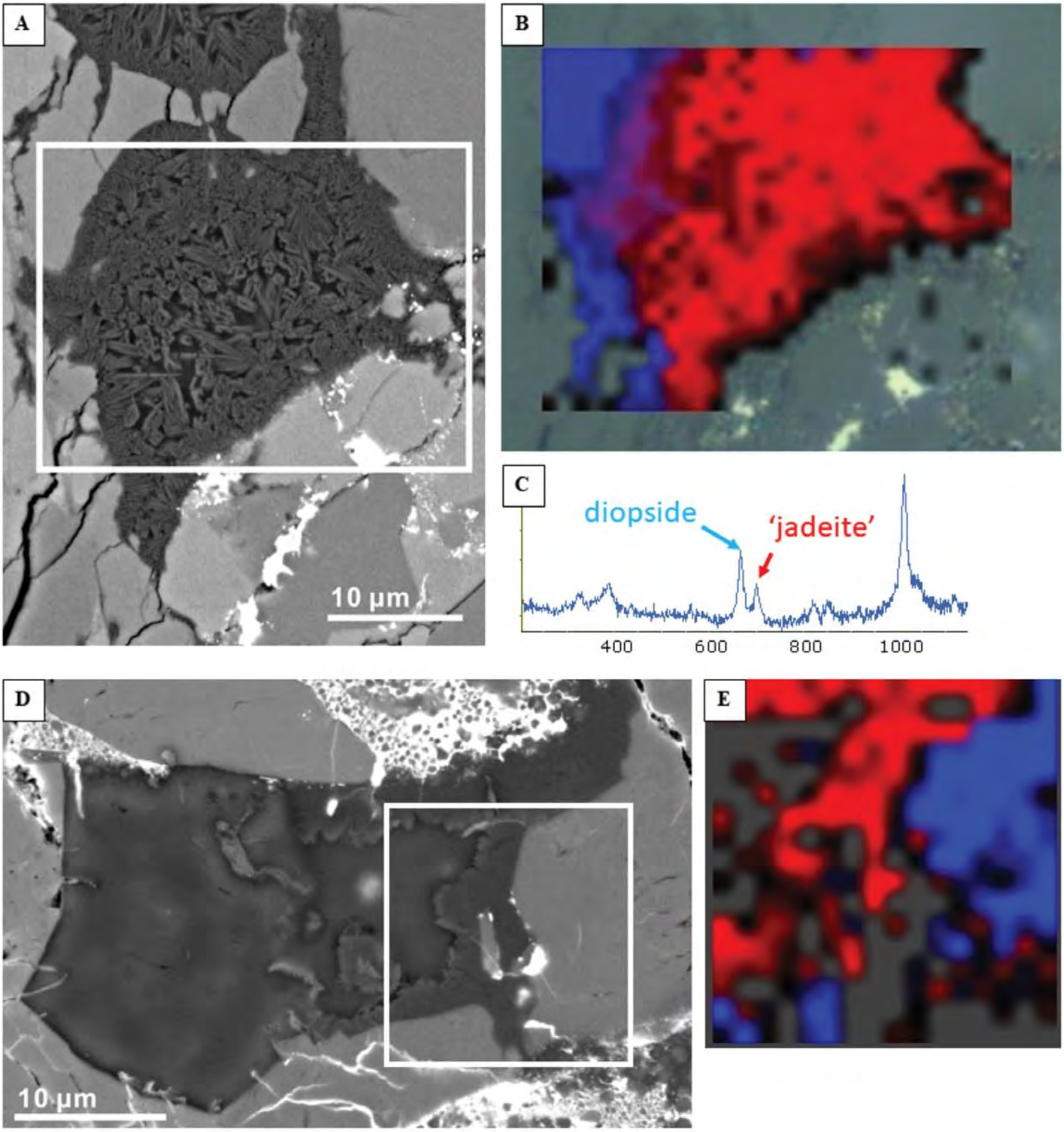

Figure 5

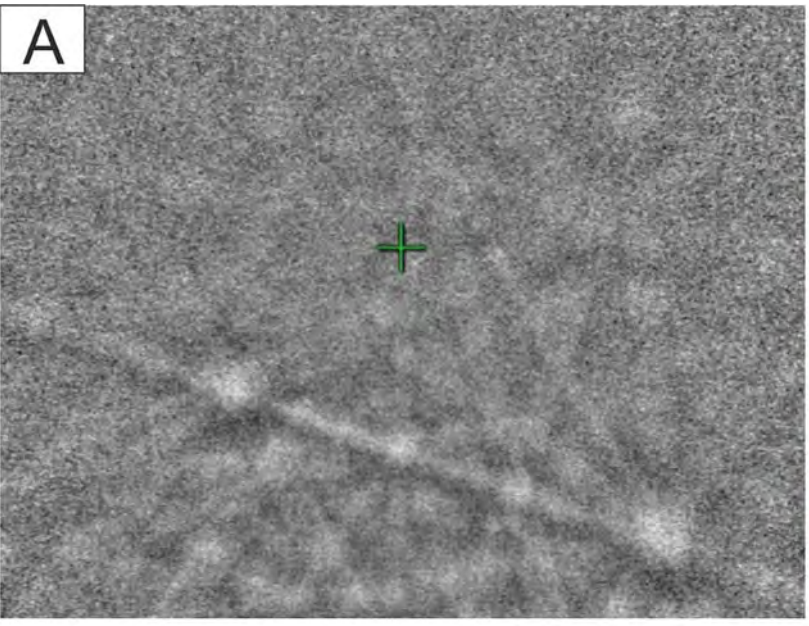
A

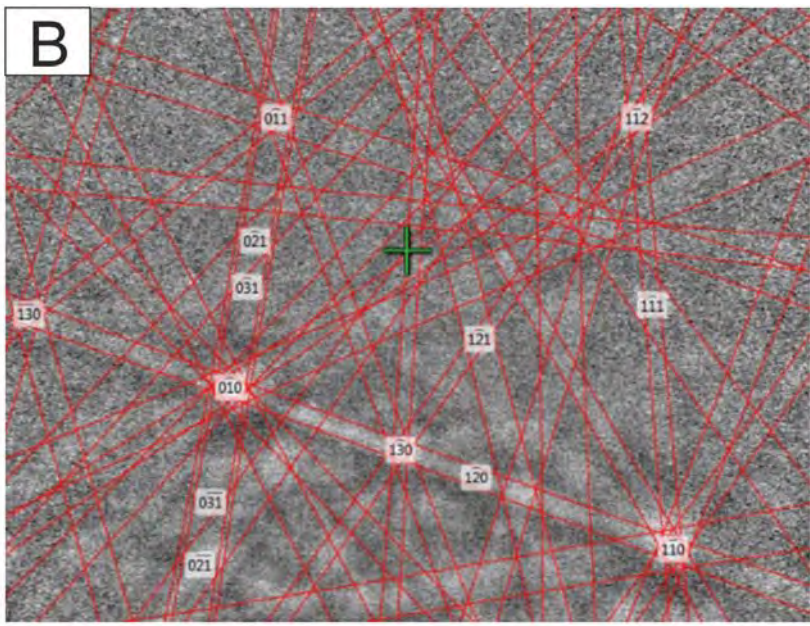
B
011
112
021
031
130
111
121
010
130
120
031
110
021

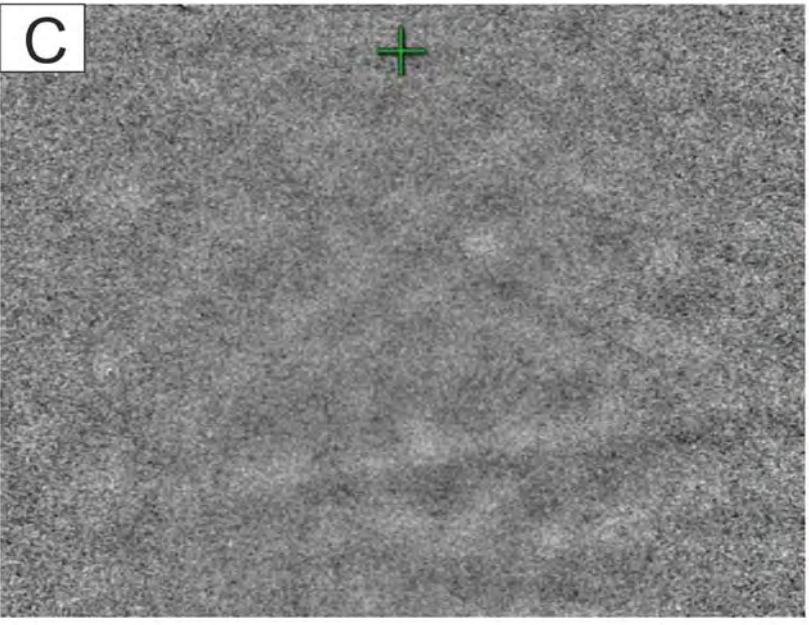
C

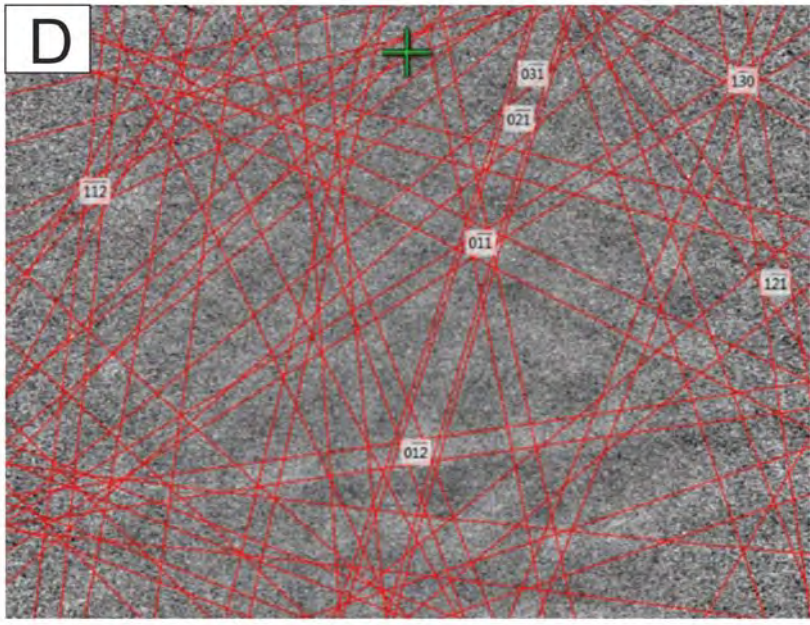
D
031
130
021
112
011
121
012

Figure 6

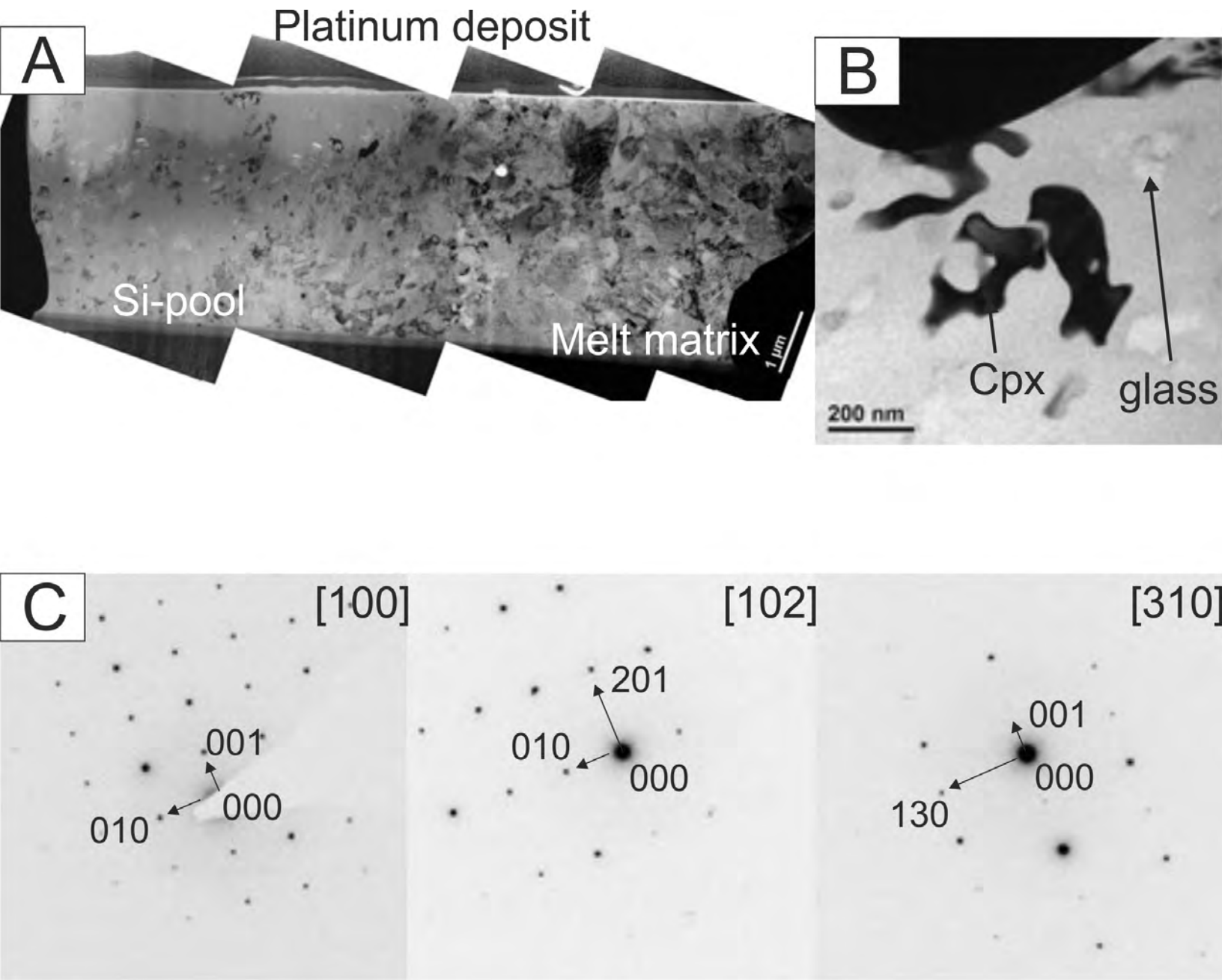
A
Platinum deposit
Si-pool
Melt matrix
1 µm
B
Cpx
glass
200 nm
C
[100]
001
000
010
[102]
201
010
000
[310]
001
000
130

Figure 7